Article

Vibration Suppression for Flexible Plate with Tunable Magnetically Controlled Joint Stiffness/Damping

Wei Hu * , **Jianming Wu, Qinghua Zhu, Jie Shen and Xunjiang Zheng**

Shanghai Aerospace Control Technology Institute, Shanghai 201109, China
* Correspondence: sjtuwhu@126.com

Abstract: Large flexible solar panels have the properties of light weight, low stiffness, and weak damping, which leads to low-frequency and large-amplitude vibrations. The existing vibration control methods of solar panels mainly adopt intelligent piezoelectric structures. However, the disadvantage is that the large stroke drive and control are limited. In the present study, a semi-active vibration control approach is proposed for flexible space solar panels based on magnetically controlled joints. The magnetic stiffness comes from the linear relationship between the joint output torque and rotation angle. The magnetic damping stems from the eddy current damping resulting from the relative motion between the permanent magnet rotor and the stator core of the joint. Firstly, the coupling dynamic modeling of a flexible plate and magnetic joints is established by adopting the Lagrange equation and the assumed mode approach. Secondly, semi-active vibration control simulations of the coupled system are performed. Meanwhile, the influence of the variable joint stiffness on the system frequency-shift effect is studied. Finally, the experimental platform is built, and simultaneously, non-contact permanent magnets and airflow are used to simulate single- and multi- frequency excitations, respectively. The experimental results indicate that, in the range of 0.06–0.343 Hz, magnetic damping is the leading factor with magnetic stiffness being the auxiliary. Additionally, it is also experimentally verified that the dual joint actuation has good synchronization. This study provides a new solution for the low-frequency vibration control of large flexible space structures.

Keywords: flexible plate; low-frequency vibration suppression; magnetically controlled joint stiffness/damping; non-contact excitations

1. Introduction

Due to the light weight, low stiffness, low fundamental frequency, and small damping of large-span structures in space, flexible solar panels are very vulnerable to suffering from vibrations due to external interference in microgravity environment. However, the vibration control of flexible structures is a difficult problem in the aerospace field. Such structures are large and complex and have constraints in aerospace applications concerning volume, mass, power consumption, and the installation of vibration control devices. Additionally, the special requirements of aerospace structures, particularly in the space environment, make vibration control challenging in theory and engineering [1–6]. Therefore, exploring new vibration suppression methods for flexible space structures has significance and practical value.

Currently, there exists passive, active, and semi-active control for solar panel vibrations.

Passive suppression does not consume satellite energy and is easy to achieve. Herein, the vibration is isolated by energy consumption. By redesigning the material and structure, the stiffness and structural damping of flexible structures are regulated, and then the excitation effect on them is reduced [7–10]. The damper on the Hubble Space Telescope can be regarded as a representative use of the passive vibration reduction of solar array [8]. A titanium alloy viscoelastic damper is installed between the solar array and its driving shaft.

The shear deformation of the damping layer is adopted to dissipate the vibration energy and then to suppress the low-frequency vibration of solar panels. Kienholz et al. [9] proposed a passive eddy current tuned mass damper (TMD), which uses non-contact magnetic eddy current buffer for energy dissipation to hinder the low- and ultra-low-frequency solar panel vibrations. Furthermore, Sales et al. [10] proposed a passive control strategy using shunted piezoelectric transducers with the purpose of suppressing vibration.

The passive method can achieve a vibration suppression effect to an extent [11,12]. However, it is challenging to satisfy the vibration control demands of flexible space structures because of its poor adaptability to variable conditions and inflexible control. Especially, low-frequency vibrations (less than 1 Hz) with a large amplitude are difficult to suppress by passive methods [13–16].

Unlike passive control, active control has the advantages of flexible control and robust adaptability for low-frequency vibration. In recent years, researchers have used smart piezoelectric structures to inhibit the vibration of solar arrays. Abdeljaber et al. [17] proposed a neural network controller with a new Kalman filter to suppress the bending and torsional modes of a cantilever plate using piezoelectric actuators. Qiu et al. [18] proposed a radial basis function neural network (RBFNN) control algorithm in order to suppress the low-frequency vibration of hinged plates with the use of piezoelectric actuators. Li et al. [19] proposed a smart embedded piezoelectric stack for a scaled solar array model, aiming to investigate the decentralized vibration control of intelligent structures. Xu et al. [20] proposed an online learning fuzzy control method based on intelligent piezoelectric structures for controlling the vibration of the cantilever. Xie et al. [21] proposed a low-order online data-driven control method combined with piezoelectric macro-fiber composite (MFC) actuators to suppress the vibration of a flexible cantilever beam. Wang et al. [22] proposed a coupling control strategy involving an adaptive sliding mode controller and a piezoelectric positive position feedback controller in order to realize the cooperative control of spacecraft attitude motion and structural elastic vibration, respectively. Gol et al. [23] proposed a method to control the bending and free vibration response of intelligent epoxy composite beams using shape memory alloy (SMA) wire actuators. Compared with the electromagnetic joint proposed in this paper, the SMA wire actuator has the advantages of a simpler structure, smaller volume, lighter weight and lower power supply, but its disadvantage is the lower response speed. Gohari et al. [24] developed a Levi-type analytical solution to describe the static and dynamic deformation response of smart laminated piezoelectric composite plates. Compared with only considering the bending deformation of the plate under low-frequency excitation below 1 Hz in this paper, their method considers not only the bending behavior of the plate, but also the torsional behavior of the plate, thus it has the advantage of accurately predicting the vibration response of the plate under arbitrary excitations.

The above active methods adopt the intelligent piezoelectric structure and then combine them with modern control theory to control vibration. Although smart materials are beneficial for the micro-amplitude drive, they have a limited drive and control in large strokes. For example, the integrated intelligent piezoelectric structure on the surface of solar panels can efficiently suppress low-frequency and small-amplitude vibration. However, because of its limited control output ability, it is only suitable for small-amplitude vibration suppression. Additionally, the multi-body structure, rigid–flexible coupling, and combined bending–torsion vibration lead to a higher dimensional system and challenging controller design. This method also needs numerous sensors on the structure to obtain the system's information. However, the surface of the solar array is covered with solar cells, and it does not allow the arbitrary installation of intelligent structures on the surface. To summarize, due to the special limitations of volume, weight and installation requirements in aerospace applications, this method is difficult to popularize and apply to spacecraft [25–31].

Semi-active control is a parameter control technology. The stiffness, inertia, and damping characteristics of specific links in the system can be regulated in real time according to their input change and output requirement. Semi-active control provides excellent

vibration characteristics. The required actuator consumes less energy and has a low price. Generally, both its volume and weight are easy to accept [32–34]. Zhang et al. [35] proposed a rotating magneto-rheological damper, which was installed between the driving mechanism and support frame of solar array, to suppress the driving disturbance caused by a solar array subject to drive fluctuation. By adjusting the coil current and damping torque and changing the magnetic field strength, semi-active vibration control of the system was realized. In addition, Hu et al. [36] proposed an active joint mechanism and semi-active vibration control method for low-frequency vibration control, and preliminarily studied the influence of joint torsional stiffness on the low-frequency vibration characteristics of two flexible beams.

In the current study, a flexible solar panel system with magnetic joints is proposed. The magnetic joint has the characteristics of the integration of structure and function. As a structural member, it provides rigid support for adjacent solar panels. As a functional element, its stiffness/damping can be actively adjusted, which can solve the frontier problem of low-frequency and large-amplitude vibration control of flexible space solar panels. The magnetic joints work based on the idea of the electromagnetic direct drive. The joint output shaft is coupled directly with the load for the driving output, which omits the traditional intermediate transmission link (gear reducer, etc.), thereby eliminating the errors in the driving process, such as elastic deformation, transmission clearance, friction vibration, etc. Therefore, the accurate and rapid adjustment of joint stiffness/damping can be realized. The multiple magnetic joints need to act simultaneously to hinder the low-frequency vibration of flexible solar panels under multi-source excitations in space. In addition, there is no need to add any intelligent structure on the surface of the solar panels, which meets the special requirements of aerospace application.

2. System Model

Figure 1 illustrates the structure configuration diagram of the coupling system of dual joints and a single flexible plate, where the xy plane is perpendicular to the plate surface. As a structural and functional component, the magnetic joints not only provide rigid support for the coupling system, but also realize the vibration control of the flexible plate. The magnetic joint can drive the flexible plate to produce rigid body motion along the rotation direction around the z-axis, and then suppress the vibration of the plate.
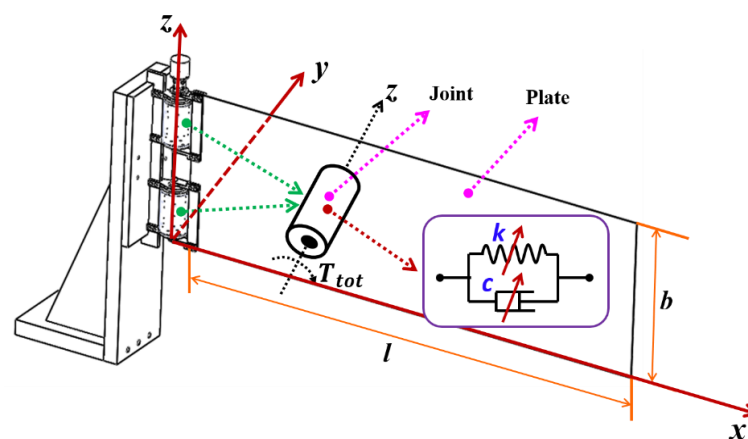

Figure 1. Configuration of the coupling system of dual joints and single flexible plate.

In terms of practical application, according to the vibration frequency and amplitude of the flexible plate, the torsional stiffness k and eddy current damping c of the magnetic joint can be actively adjusted.

2.1. Principle of Tunable Magnetically Controlled Stiffness/Damping

(a)   Tunable magnetically controlled stiffness.

The magnetic stiffness k comes from that, with the coils being loaded with DC power, the joint output torque is almost linearly proportional to the rotation angle. The equivalent magnetic stiffness is expressed as follows:

$$k = \frac{dT_{drive}}{d\theta} \tag{1}$$

where T_{drive} and θ represent the driving torque and rotation angle of the joint, separately. For further details about the driving torque T_{drive}, please see reference [36].

(b)   Tunable magnetically controlled damping.

The magnetic damping c comes from the eddy current damping resulting from the relative motion between the permanent magnet rotor and the stator core of the joint. The equivalent magnetic damping of the joint can be controlled by actively adjusting the input current. The equivalent magnetic damping coefficient is obtained as

$$c = \frac{dT_{damp}}{d\omega} \tag{2}$$

where T_{damp} and ω represent the eddy current damping torque and rotational speed of the joint, separately. The joint damping torque T_{damp} is related to the material and structure parameters of permanent magnets and coils as well as the input current. For more details about the damping torque, please see reference [36].

However, whether it is the variable stiffness or variable damping, which contributes the most to the vibration isolation effect needs to be further explained.

On one hand, at a low frequency, although the frequency is low, the rotation angle is large. This large angle leads to a higher speed of cutting the magnetic lines in unit time. Therefore, the eddy current damping is large. When the joint is loaded with DC-2 A, the current intensity is small, resulting in a small joint torsional stiffness. However, even so, the external excitation frequency is still less compared with the system natural frequency when dual joints are loaded with DC-2 A, resulting in no obvious effect of the variable stiffness control of the system. In such a case, variable damping is considered as the main element, while variable stiffness secondary.

On the other, at high frequency, the rotation angle is small, which will lead to a lower speed of cutting magnetic lines in unit time. Therefore, the eddy current damping is small. Meanwhile, when the current increases, the joint torsional stiffness also increases. Consequently, variable stiffness is the leading element, while variable damping secondary.

Moreover, compared with the coupling system of a flexible beam and single magnetic joint in reference [34], the plate in this paper has a longer length, wider width, and higher flexibility. Meanwhile, the torsional stiffness of dual joints is greater than that of single joint. Ideally, it can better reflect the effect of joint variable stiffness vibration suppression. Furthermore, there are usually two joints between the substrates of solar panels. Therefore, this study will focus on the tunable magnetically controlled stiffness/damping semi-active vibration control of the coupling system of dual joints and a single flexible plate.

2.2. Dynamic Modeling of the Coupled System

Since the system moves on the horizontal plane, the gravity is negligible. Through employing the Lagrange method, the dynamic equation of the system should satisfy the following form:

$$\frac{d}{dt}\left(\frac{\partial L}{\partial \dot{q}_i}\right) - \frac{\partial L}{\partial q_i} + \frac{\partial D}{\partial \dot{q}_i} = Q_i, \ i = 0, 1, 2, \ldots \tag{3}$$

where L represents the Lagrange multiplier, q_i denotes generalized coordinates, D is the Rayleigh dissipated energy, and Q_i indicates the generalized force acting on the generalized coordinate q_i.

The Lagrange multiplier L can be expressed as:

$$L = T - V \tag{4}$$

where T and V represent the kinetic and potential energy of the system, separately.

Consider a coupling system of dual joints and a flexible beam in a horizontal plane, which can be found in Figure 2. Figure 2 illustrates the structural deformation diagram of the flexible plate, where the two-dimensional plate is simplified into a one-dimensional beam model. In fact, not only is the torsional rigid body motion θ shown, but also the bending deformation of the plate based on the torsional rigid body motion θ is demonstrated. The body-fixed coordinate (x, y) is introduced, aiming to efficiently depict the local deflection of the beam; the origin is at the joint. Then, in the inertial frame, the position (x, y) of a point on the deformed centerline of the beam can be expressed as:

$$\begin{cases} X = x \cos\theta - y(x, t) \sin\theta \\ Y = x \sin\theta + y(x, t) \cos\theta \end{cases} \tag{5}$$

where x indicates the location of the undeformed point on the flexible beam and $y(x, t)$ represents the transverse elastic displacements with θ denoting the angular motions of the joint.
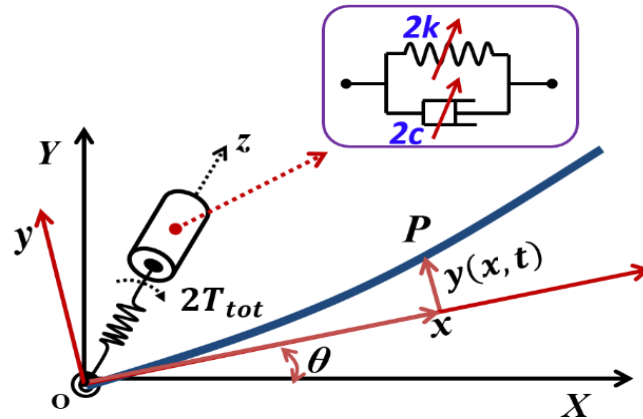

Figure 2. The simplified dynamic model for the coupling system of dual joints and single flexible plate.

According to Equation (5), we obtain

$$\begin{cases} \dot{X} = (\dot{x} \cos\theta - x\dot{\theta} \cos\theta) - (\dot{y} \sin\theta + y\dot{\theta} \cos\theta) \\ \dot{Y} = (\dot{x} \sin\theta + x\dot{\theta} \cos\theta) + (\dot{y} \cos\theta - y\dot{\theta} \sin\theta) \end{cases} \tag{6}$$

Then, the absolute velocity v at any point (x, y) on the beam can be formulated as:

$$v(x, y) = \left(\dot{X}^2 + \dot{Y}^2 \right)^{\frac{1}{2}} = \left[\left(x^2 + y^2 \right) \dot{\theta}^2 + 2(x\dot{y} - \dot{x}y)\dot{\theta} + \left(\dot{x}^2 + \dot{y}^2 \right) \right]^{\frac{1}{2}} \tag{7}$$

For $\dot{x} = 0$, the absolute velocity v can be calculated as follows:

$$v(x, y) = \left(\dot{X}^2 + \dot{Y}^2 \right)^{\frac{1}{2}} = \left[\left(x^2 + y^2 \right) \dot{\theta}^2 + 2x\dot{y}\dot{\theta} + \dot{y}^2 \right]^{\frac{1}{2}} \tag{8}$$

Ignoring the longitudinal deformation of the beam, the kinetic energy of the system is

$$
\begin{aligned}
T &= 2 \cdot \tfrac{1}{2} J \dot{\theta}^2 + \tfrac{1}{2} \int_0^l \rho A v(x,y)^2 dx \\
&= J \dot{\theta}^2 + \tfrac{1}{2} \int_0^l \rho A \left[(x^2 + y^2) \dot{\theta}^2 + 2 x \dot{y} \dot{\theta} + \dot{y}^2 \right] dx
\end{aligned}
\tag{9}
$$

where ρ refers to the density of the beam, A represents the cross-sectional area of the beam, J indicates the moment of inertia of one joint, and l denotes the length of flexible plate, as shown in Figure 1.

The potential energy of the system is

$$
V = \frac{1}{2} \int_0^l EI \left[\frac{\partial^2 y(x,t)}{\partial x^2} \right]^2 dx + 2 \cdot \frac{1}{2} k \theta^2
\tag{10}
$$

where EI indicates the bending stiffness of the beam and k represents the torsional stiffness of one joint, as shown in Equation (1).

Due to the damping characteristics of the joint mechanism, the dissipated energy of dual joints becomes

$$
D = 2 \cdot \frac{1}{2} c \dot{\theta}^2
\tag{11}
$$

where c is the damping coefficient of one joint, as shown in Equation (2). Here, in our theoretical model, only the electromagnetic damping of dual joints is considered, while the structural damping of the flexible plate is not considered. The main reason is that the damping ratio of the flexible plate is far less than that of the joint mechanism.

One can enlarge the physical displacement coordinates of the flexible beam using the assumed mode shapes,

$$
y(x,t) = \boldsymbol{\varphi}^{\mathrm{T}}(x) \mathbf{p}(t); \boldsymbol{\varphi}^{\mathrm{T}} = [\varphi_1, \varphi_2, \ldots, \varphi_n]; \mathbf{p}^{\mathrm{T}} = [p_1, p_2, \ldots, p_n]
\tag{12}
$$

where $\boldsymbol{\varphi}(x)$ represents the eigenfunction of the clamped-free cantilever beam, $\mathbf{p}(t)$ is the generalized coordinate vector of the beam, and n refers to the number of assumed modes. In addition, we merely consider the first-order mode in the simulated calculation for the beam. For the sake of convenience, it is supposed that $\varphi_1 \to \varphi$; $p_1 \to p$. For the state variables $\{\theta, p\}$, the generalized force is expressed as $\{Q_\theta, Q_p\}$.

Equation (12) can be rewritten as follows:

$$
y(x,t) = \sum_{i=1}^{N} \varphi_i(x) p_i(t) \approx \varphi_1(x) p_1(t) = \varphi(x) p(t)
\tag{13}
$$

$$
\varphi(x) = \varphi_1(x) = C_1 \sin(\beta_1 x) + C_2 \cos(\beta_1 x) + C_3 \sinh(\beta_1 x) + C_4 \cosh(\beta_1 x)
\tag{14}
$$

$$
p(x) = p_1(x) = A \cos(\omega_1 t) + B \sin(\omega_1 t)
\tag{15}
$$

where the first resonant angular frequency of cantilever beam is $\omega_1 = \beta_1^2 \sqrt{\frac{EI}{\rho A}}$, which can be obtained by the differential equation of free vibration of cantilever beam. The parameters A and B can be obtained from the initial conditions of vibration. The four parameters C_1, C_2, C_3 and C_4 can be obtained by the cantilever beam with one end constrained and one end free.

For $x = 0$

$$
y(0,t) = 0, \quad \frac{\partial y(0,t)}{\partial x} = 0
\tag{16}
$$

For $x = l$

$$
EI \frac{\partial^2 y(l,t)}{\partial x^2} = 0, \quad EI \frac{\partial^3 y(l,t)}{\partial x^3} = 0
\tag{17}
$$

According to reference [37], the first-order mode eigenfunction of cantilever beam can be expressed as follows:

$$\varphi(x) = \varphi_1(x) = \sin(\beta_1 x) - \sinh(\beta_1 x) - \frac{\sinh(\beta_1 l) + \sin(\beta_1 l)}{\cosh(\beta_1 l) + \cos(\beta_1 l)}[\cos(\beta_1 x) - \cosh(\beta_1 x)] \tag{18}$$

where $\beta_1 = \frac{1.875}{l}$.

Therefore, based on the mode shapes together with the generalized coordinates in Equation (13), the kinetic energy T in Equation (9) and the potential energy V in Equation (10) can be rewritten as:

$$
\begin{aligned}
T = J\dot{\theta}^2 + & \left\{ \left[\tfrac{1}{2}\rho A \int_0^l x^2 dx\right] + \left[\tfrac{1}{2}\rho A \int_0^l \varphi^2(x)dx\right] p^2 \right\}\dot{\theta}^2 \\
& + \left[\rho A \int_0^l x\varphi(x)dx\right]\dot{p}\dot{\theta} + \left[\tfrac{1}{2}\rho A \int_0^l \varphi^2(x)dx\right]\dot{p}^2
\end{aligned}
\tag{19}
$$

$$V = \left\{ \frac{1}{2}EI \int_0^l \left[\frac{\partial^2 \varphi(x)}{\partial x^2}\right]^2 dx \right\} p^2 + 2 \cdot \frac{1}{2}k\theta^2 = \left[\frac{1}{2}\rho A \int_0^l \varphi^2(x)dx\right]\omega_1^2 p^2 + k\theta^2 \tag{20}$$

For generalized coordinate θ, based on the Lagrange equation Equations (3) and (4), we have:

$$\frac{d}{dt}\left(\frac{\partial T}{\partial \dot{\theta}}\right) - \frac{\partial T}{\partial \theta} + \frac{\partial V}{\partial \theta} + \frac{\partial D}{\partial \dot{\theta}} = Q_\theta \tag{21}$$

where

$$
\begin{aligned}
\frac{\partial T}{\partial \dot{\theta}} &= \left\{ 2J + \left[\rho A \int_0^l x^2 dx\right] + \left[\rho A \int_0^l \varphi^2(x)dx\right] p^2 \right\}\dot{\theta} + \left[\rho A \int_0^l x\varphi(x)dx\right]\dot{p} \\
\frac{d}{dt}\left(\frac{\partial T}{\partial \dot{\theta}}\right) &= \left\{ 2J + \left[\rho A \int_0^l x^2 dx\right] + \left[\rho A \int_0^l \varphi^2(x)dx\right] p^2 \right\}\ddot{\theta} + 2\left[\rho A \int_0^l \varphi^2(x)dx\right]\dot{\theta}\dot{p}p \\
& \quad + \left[\rho A \int_0^l x\varphi(x)dx\right]\ddot{p} \\
\frac{\partial T}{\partial \theta} &= 0, \\
\frac{\partial V}{\partial \theta} &= 2k\theta, \\
\frac{\partial D}{\partial \dot{\theta}} &= 2c\dot{\theta}
\end{aligned}
\tag{22}
$$

Then, we obtain

$$
\begin{aligned}
& \left\{ 2J + \left[\rho A \int_0^l x^2 dx\right] + \left[\rho A \int_0^l \varphi^2(x)dx\right] p^2 \right\}\ddot{\theta} + \left[\rho A \int_0^l x\varphi(x)dx\right]\ddot{p} \\
& + 2k\theta + 2c\dot{\theta} + 2\left[\rho A \int_0^l \varphi^2(x)dx\right]\dot{\theta}\dot{p}p = Q_\theta
\end{aligned}
\tag{23}
$$

For generalized coordinate p, based on the Lagrange equation Equations (3) and (4), we have:

$$\frac{d}{dt}\left(\frac{\partial T}{\partial \dot{p}}\right) - \frac{\partial T}{\partial p} + \frac{\partial V}{\partial p} + \frac{\partial D}{\partial \dot{p}} = Q_p \tag{24}$$

where

$$
\begin{aligned}
\frac{\partial T}{\partial \dot{p}} &= \left[\rho A \int_0^l x\varphi(x)dx\right]\dot{\theta} + \left[\rho A \int_0^l \varphi^2(x)dx\right]\dot{p} \\
\frac{d}{dt}\left(\frac{\partial T}{\partial \dot{p}}\right) &= \left[\rho A \int_0^l x\varphi(x)dx\right]\ddot{\theta} + \left[\rho A \int_0^l \varphi^2(x)dx\right]\ddot{p} \\
\frac{\partial T}{\partial p} &= \left[\rho A \int_0^l \varphi^2(x)dx\right]\dot{\theta}^2 p \\
\frac{\partial V}{\partial p} &= \left[\rho A \int_0^l \varphi^2(x)dx\right]\omega^2 p \\
\frac{\partial D}{\partial \dot{p}} &= 0
\end{aligned}
\tag{25}
$$

Then, we obtain

$$\left[\rho A \int_0^l x\varphi(x)dx\right]\ddot{\theta} + \left[\rho A \int_0^l \varphi^2(x)dx\right]\ddot{p} + \left[\rho A \int_0^l \varphi^2(x)dx\right]\omega^2 p$$
$$- \left[\rho A \int_0^l \varphi^2(x)dx\right]\dot{\theta}^2 p = Q_p \tag{26}$$

Equations (23) and (26) can be rewritten in matrix form:

$$\begin{bmatrix} M_{11} & M_{12} \\ M_{12} & M_{22} \end{bmatrix}\begin{Bmatrix} \ddot{\theta} \\ \ddot{p} \end{Bmatrix} + \begin{bmatrix} 2k & 0 \\ 0 & (2B_2\omega^2) \end{bmatrix}\begin{Bmatrix} \theta \\ p \end{Bmatrix} + \begin{bmatrix} 2c & 0 \\ 0 & 0 \end{bmatrix}\begin{Bmatrix} \dot{\theta} \\ \dot{p} \end{Bmatrix} + \begin{Bmatrix} H_1 \\ H_2 \end{Bmatrix} = \begin{Bmatrix} Q_\theta \\ Q_p \end{Bmatrix} \tag{27}$$

where $M_{ij}, i,j = 1,2$ are obtained based on the coupling effect between rigid motions and elastic modes, and H_i, $i = 1,2$ indicate the nonlinear forces. The generalized external interference is $\{M_\theta sin(2\pi ft), 0\}$. The relevant items M_{ij}, H_i in Equation (27) are:

$$M_{11} = 2J + 2B_1 + 2B_2p^2, \qquad M_{12} = B_3, \qquad M_{22} = 2B_2 \tag{28}$$

$$B_1 = \frac{1}{2}\rho A \int_0^l x^2 dx, \qquad B_2 = \frac{1}{2}\rho A \int_0^l \varphi^2(x)dx, \qquad B_3 = \rho A \int_0^l x\varphi(x)dx \tag{29}$$

$$H_1 = \dot{\theta}\dot{p}(4B_2p), \qquad H_2 = -\dot{\theta}^2(2B_2p) \tag{30}$$

The dynamic model considers the torsional stiffness and damping of the joint mechanism, so this model can be used to effectively predict the dynamic characteristics of the system.

3. Numerical Analysis and Simulation

According to the dynamic model in Section 2, the numerical simulations were performed. Table 1 shows the geometrical and material parameters of the aluminum plate. Additionally, in this study, we did not consider the structural damping of the plate. The length of the flexible plate remained unchanged and the stiffness of dual joints was adjustable. Figure 3 depicts the first two natural frequencies of the system in relation to the torsional stiffness of dual joints. When the torsional stiffness increases from 0 to $6\,N \cdot m/rad$, the first and second resonant frequencies of the system increase from 0 to 0.5354 Hz and from 7.004 to 7.787 Hz, respectively.

Table 1. Structural and material parameters of the system.

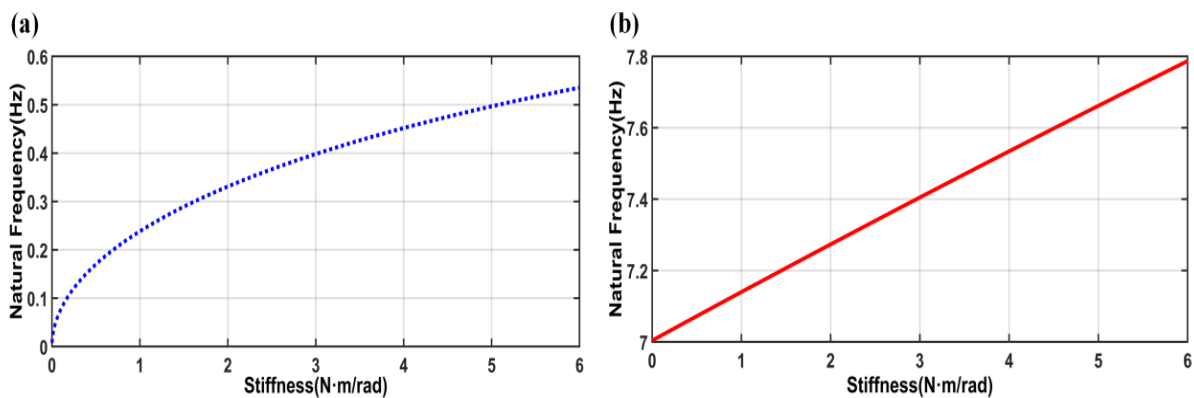| Length (*l*)	Thickness (*h*)	Width (*b*)	Elastic Modulus (*E*)	Density (*ρ*)
1000 mm	1.5 mm	310 mm	69 GPa	2766 kg/m^3

Figure 3. Natural frequency of the system changes with joint torsional stiffness. (**a**) 1st order; (**b**) 2nd order.

Figure 4 presents the frequency response of the system under varying current intensities. In Table 2, when the electric current increases from 1 to 6 A, the joint torsional stiffness increases from 0.38 to 2.31 N · m/rad, and the first resonant frequency increases from 0.21 to 0.48 Hz. Moreover, the resonance peak decreases from 54.27° to 23.74°.
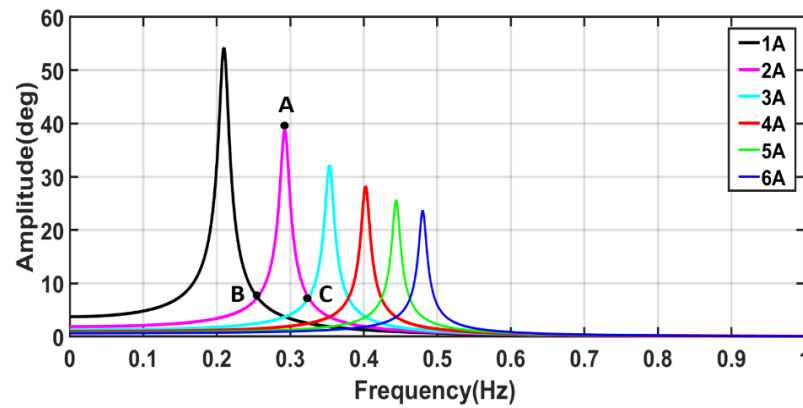

Figure 4. Frequency response of the system.

Table 2. Variable stiffness control effect of the system.

Current (A)	Torsional Stiffness (N · m/rad)	Natural Frequency (Hz)	Amplitude (°)
1	0.3843	0.210	54.27
2	0.7686	0.292	38.89
3	1.153	0.353	32.24
4	1.537	0.402	28.28
5	1.922	0.444	25.67
6	2.306	0.480	23.74

In Figure 5, the comparison of the system frequency-shift effect is presented under different conditions: single joint and dual joints. Overall, the system natural frequency with dual joints is less than that with one joint. The reason is that although the torsional stiffness increases for dual joints, the load also increases. Therefore, the frequency shift of the variable stiffness caused by the increased load is much greater than that caused by the increased torsional stiffness.
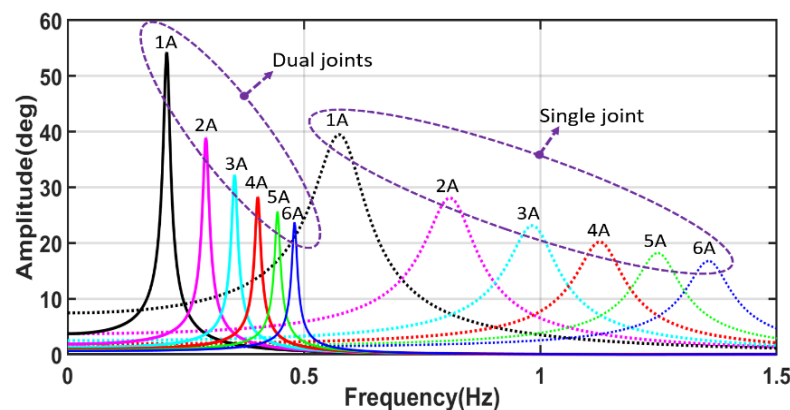

Figure 5. Comparison of system frequency-shift effect under different conditions: single joint and dual joints.

With the joint torsional stiffness being changed at the resonant peak, the vibration suppression effect is most obvious. Therefore, it can be supposed that the exciting frequency is the first natural frequency of the system when the joint receives DC-2 A power. Figure 6a shows the time domain response of the system when the external excitation frequency is 0.292 Hz, corresponding to the point A in Figure 4, and when the joint torsional stiffness is 0.7686 N · m/rad in Table 2. In Figure 6a, the exciting frequency is the first natural frequency of the system under DC-2 A, the resonance appears, and then the angle amplitude reduces from 38.89° (0 A) to 1.88° (4 A) and 0.97° (6 A), and the vibration isolation can be realized by the frequency-shifting phenomenon.
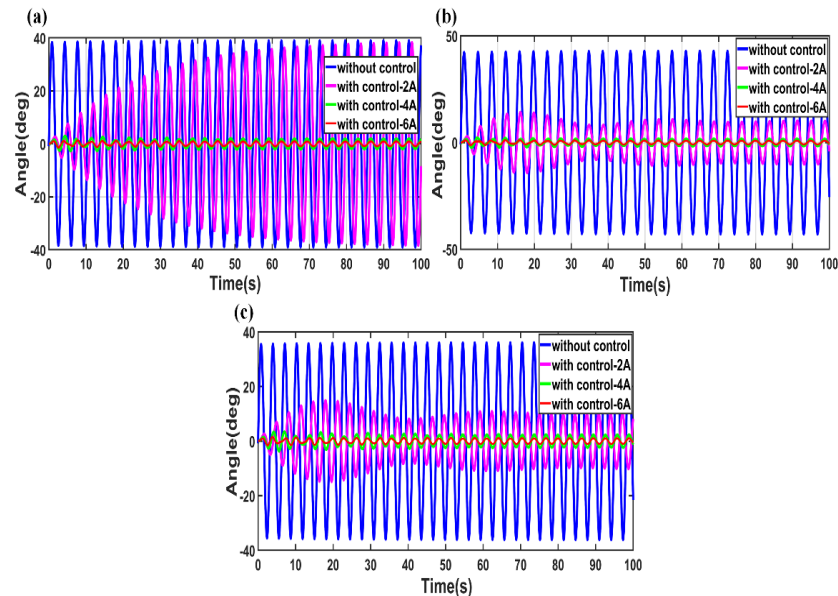

Figure 6. Time domain response of the system excitation at (**a**) 0.292 Hz, (**b**) 0.266 Hz and (**c**) 0.316 Hz.

Furthermore, as shown in Figure 4, we see the external excitation frequency of 0.266 Hz (point B) and 0.316 Hz (point C) near 0.292 Hz (point A). In Figure 6b, the external excitation frequency reaches 0.266 Hz, and the angle of magnitude lowers from 42.78° (0 A) to 9.904° (2 A), 1.61° (4 A) and 0.88° (6 A). In Figure 6c, the excitation frequency reaches 0.316 Hz, and the angular amplitude lowers from 35.93° (0 A) to 9.964° (2 A) to 2.33° (4 A) and 0.98° (6 A). It is important to note that, although the points B and C are not at the resonance peak, the increase in joint torsional stiffness causes the system resonance frequency to shift (or increase), causing the points B and C to produce a certain vibration isolation effect, as shown in Figure 6b,c.

In Figure 7, when DC-2 A current is continuously applied to both joints, the system maintains a certain torsional stiffness constraint throughout. The external excitation frequency is located on the right side of the system resonance frequency when DC-2 A is applied. It is demonstrated that the higher the external excitation frequency is, the smaller the joint rotation angle is.
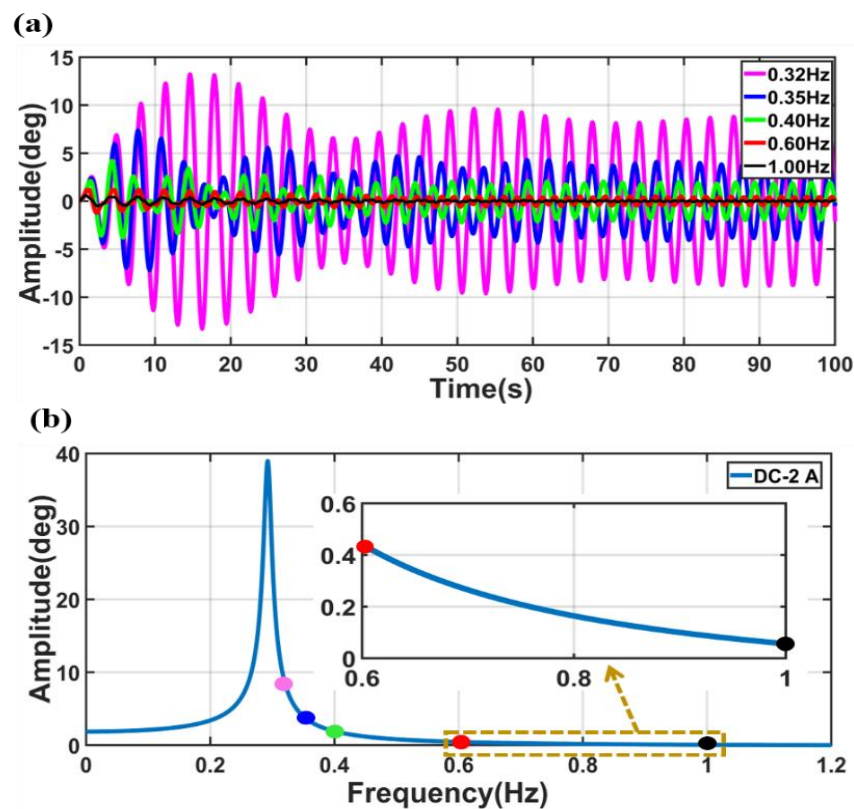
Figure 7. Comparative results of rotation angle response excitation at higher frequency. (**a**) Time domain response; (**b**) Frequency domain response.

In Figure 8, when a DC-6 A current power supply is applied to both joints, the first eight modes of the system are performed. In Figure 8, the first mode (0.48 Hz) is dominated by the rigid body motion, supplemented by the bending deformation of the plate, and the rigid body moves in the same direction as the bending deformation of the plate. The second mode is the bending mode (5.47 Hz), and the third mode is the coupled bending–twisting and vibration mode (8.51 Hz). After the third mode, the modal frequency is higher. However, in this study, we mainly focused on the low-frequency vibration below 1 Hz, not on the high-order modes above 1 Hz, thereby leaving only the rigid body mode and pure bending mode. Therefore, in this study, it is reasonable to simplify the two-dimensional plate into a one-dimensional beam.
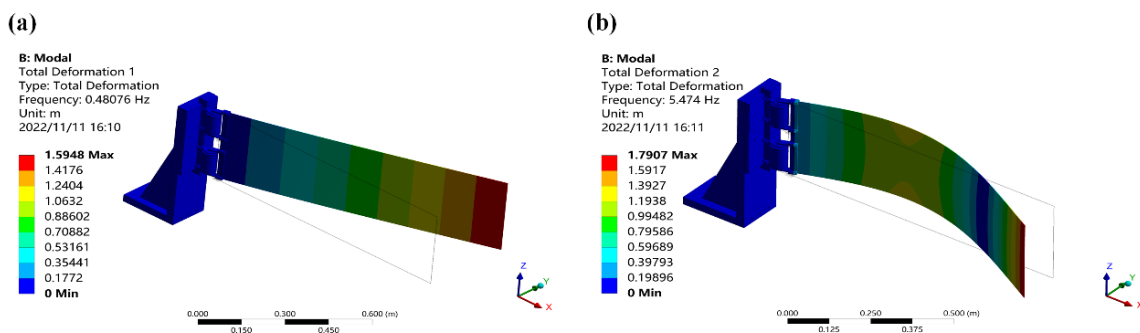

Figure 8. *Cont.*
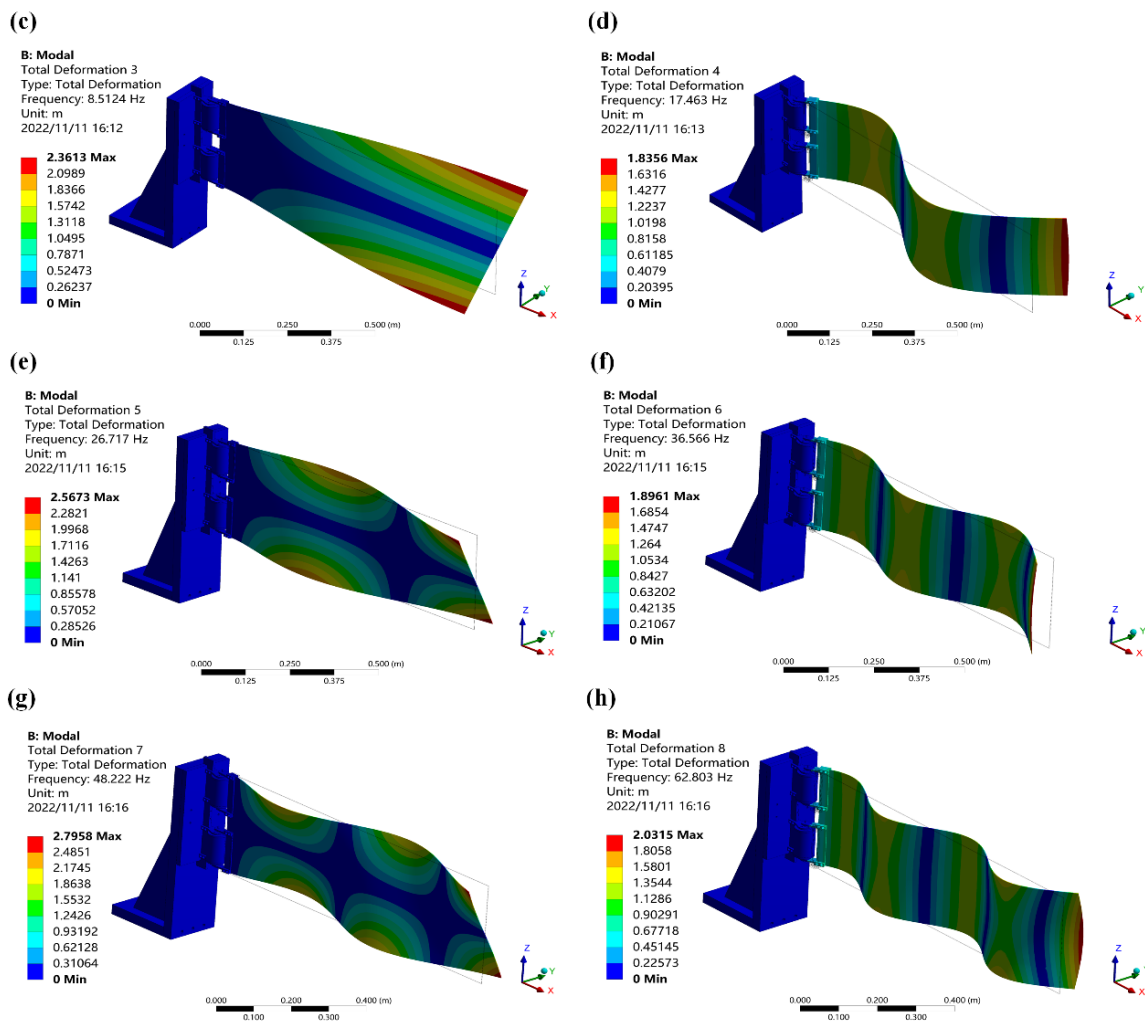
Figure 8. Mode shape of the system: (**a**) 1st order, (**b**) 2nd order, (**c**) 3rd order, (**d**) 4th order, (**e**) 5th order, (**f**) 6th order, (**g**) 7th order and (**h**) 8th order.

4. Experiment Results and Discussion

4.1. Experimental Device

This study used two kinds of non-contact excitation methods to simulate single- and multi-frequency excitations. The experimental device is shown in Figure 9.
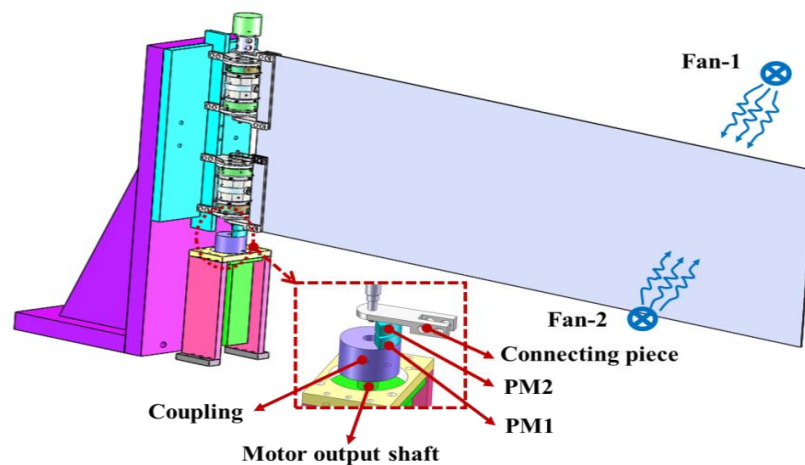

Figure 9. Configuration of dual joints and one flexible plate.

The vibration control experiments under the non-contact periodic single-frequency excitations were performed. These experiments were under the conditions of **case-1** (same frequency but diverse amplitudes) and **case-2** (diverse frequencies and diverse amplitudes). The experimental platform is shown in Figure 10. Herein, the selected aluminum plate is larger and more flexible than the previous flexible beam [34]. The excitation frequency is regulated by the motor rotation speed. By adjusting the moving slide table up and down, the magnetic excitation air gap can be adjusted. By changing the intensity of the excitation magnetic fields between the air gaps, diverse excitation amplitudes can be generated.
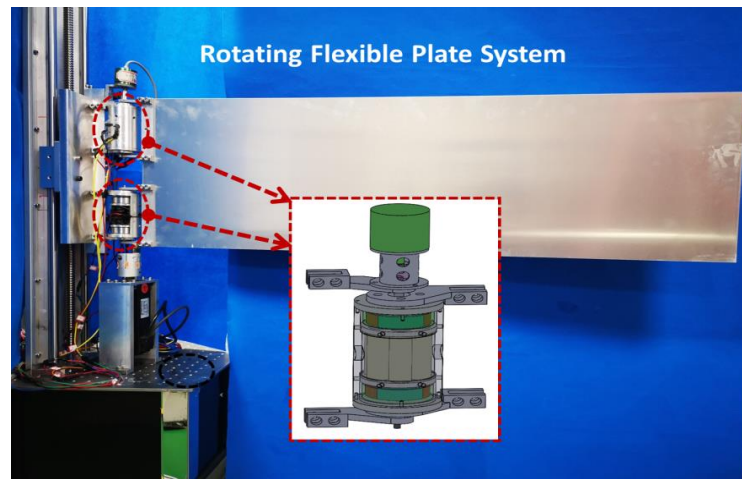

Figure 10. Schematic diagram of experimental device.

4.2. Vibration Control Experiments Based on Single Frequency Excitation

4.2.1. **Case-1**: Same Frequency yet Diverse Amplitudes

Three groups of experiments were performed at the same frequency yet diverse amplitudes. The semi-active vibration control effects are shown in Figure 11, which are summarized in Table 3. The disturbance frequency reaches 0.23 Hz with a disturbance amplitude of about 9~12°. After the dual joint semi-active control, the vibration reduction effect of 14.56–19.64 dB can be achieved.

Table 3. Vibration control effect based on the same frequency yet diverse amplitudes excitation.

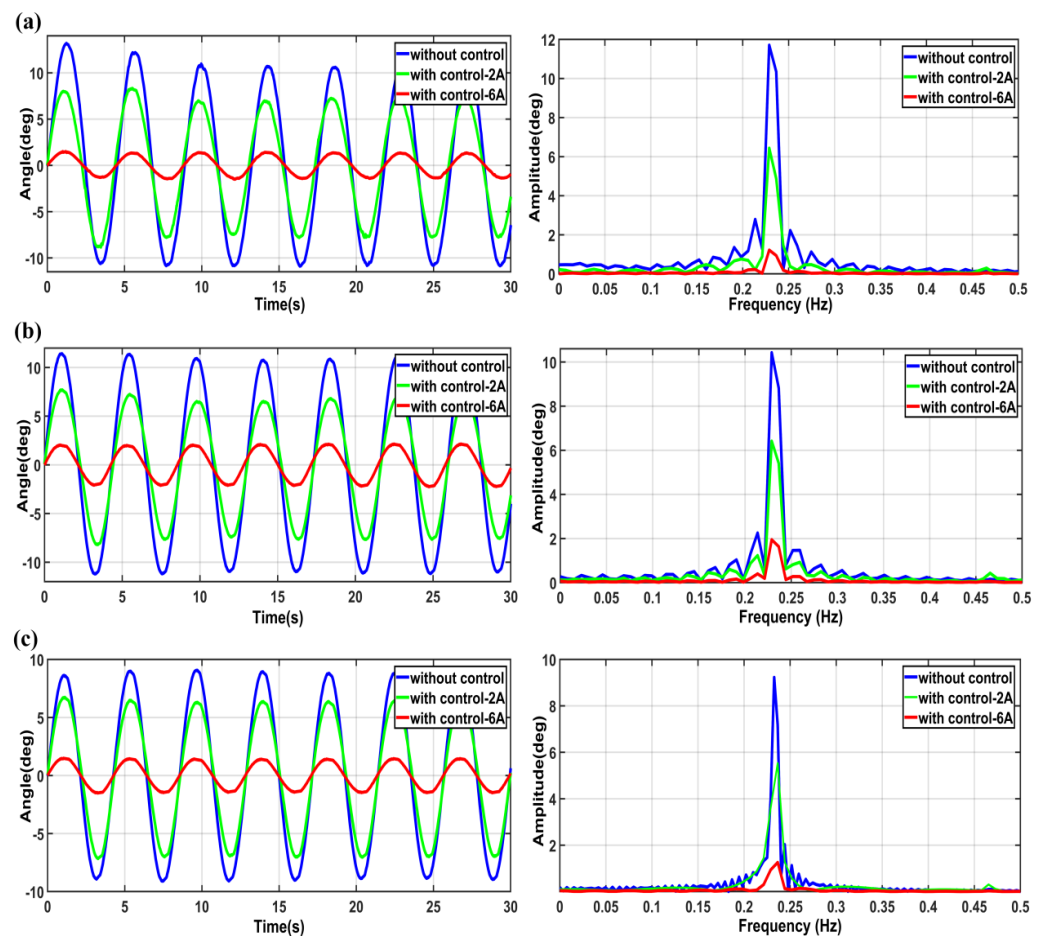| Major Frequency			Amplitude	
			Without control	With control-6 A
I	0.23 Hz	Time domain	−10.84~13.19°	−1.48~1.48°
		Frequency domain	11.71°	1.22°
		Control effect	89.58% (−19.64 dB)	
			Without control	With control-6 A
II	0.23 Hz	Time domain	−11.18~11.42°	−2.11~2.10°
		Frequency domain	10.43°	1.95°
		Control effect	81.30% (−14.56 dB)	
			Without control	With control-6 A
III	0.23 Hz	Time domain	−8.92~8.98°	−1.51~1.46°
		Frequency domain	9.23°	1.26°
		Control effect	86.35% (−17.30 dB)	

Figure 11. Vibration control experiments based on the same frequency yet diverse amplitude excitations at 0.23 Hz. (**a**) interference amplitude of 11.71°; (**b**) interference amplitude of 10.43°; (**c**) interference amplitude of 9.23°.

4.2.2. **Case-2**: Diverse Frequencies and Diverse Amplitudes

In Figure 12, the vibration control effects under diverse frequency and diverse amplitude excitations are shown. The three groups of experimental findings are presented in Table 4. According to the experimental results, the interference frequency is within 0.244~0.343 Hz and the interference amplitude is within 3.5~8.4°. After the dual joint control, the vibration reduction effect can reach 15.23–18.63 dB.

To summarize, in the case of single-frequency excitations (**case-1** and **-2**), the interference frequency was 0.23–0.343 Hz. Normally, with the external excitation frequency being the first natural frequency of the system, the vibration suppression effect is most obvious. However, herein the external excitation frequency was less when compared with the natural frequency of the system, when dual joints are loaded with DC-2 A, resulting in no obvious effect of the magnetic stiffness control of the system. Therefore, magnetic damping was the major contributor, while magnetic stiffness was the auxiliary. Furthermore, it was also experimentally verified that the dual joint actuation had good synchronization.
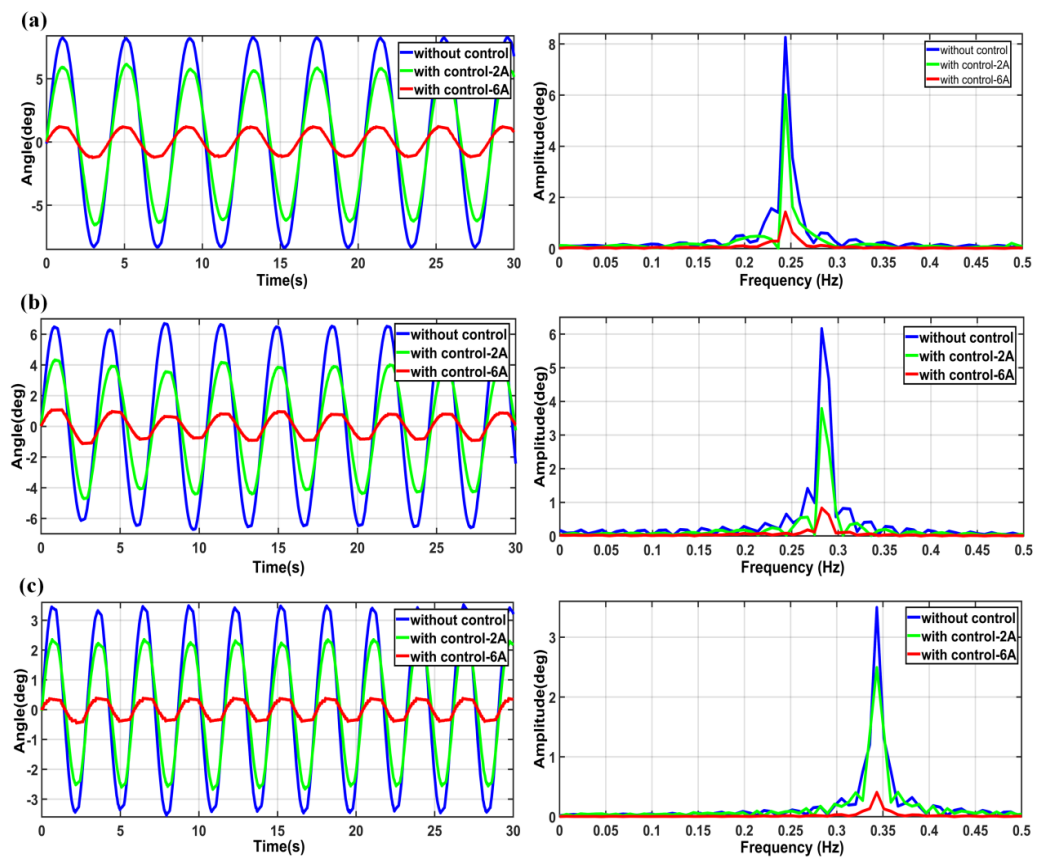
Figure 12. Vibration control experiments based on diverse frequency and diverse amplitude excitations at (**a**) 0.244 Hz, (**b**) 0.282 Hz and (**c**) 0.343 Hz.

Table 4. Vibration control effect based on diverse frequency and diverse amplitude excitations.

Major Frequency		Amplitude		
			Without control	With control-6 A
I	0.244 Hz	Time domain	−8.36~8.22°	−1.25~1.22°
		Frequency domain	8.26°	1.43°
		Control effect	82.69% (−15.23 dB)	
			Without control	With control-6 A
II	0.282 Hz	Time domain	−6.71~6.68°	−1.13~1.07°
		Frequency domain	6.16°	0.83°
		Control effect	86.52% (−17.41 dB)	
			Without control	With control-6 A
III	0.343 Hz	Time domain	−3.52~3.49°	−0.45~0.39°
		Frequency domain	3.50°	0.41°
		Control effect	88.29% (−18.63 dB)	

4.3. Vibration Control Experiments Based on Multiple Frequency Excitations

Multi-frequency excitations were simulated by fan airflow, acting on the surface of flexible plate. Three groups of experiments were carried out. The vibration suppression effects are shown in Figure 13 and summarized in Table 5.
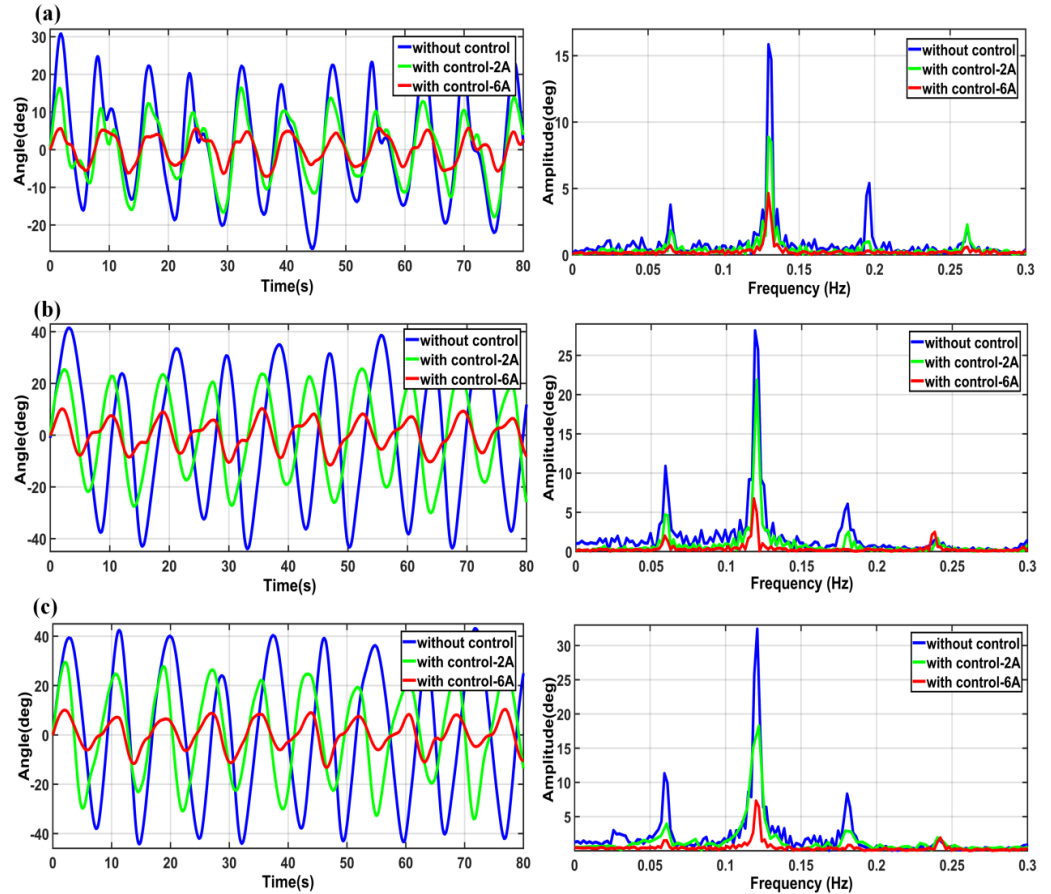

Figure 13. Vibration control experiments: (**a**) Experiment I, (**b**) Experiment II and (**c**) Experiment III.

Table 5. Vibration control effect based on fans airflow excitation.

Experiment	Amplitude		Major Frequency		
I	Without control	−26.27~30.78°		0.06 Hz	0.13 Hz	0.19 Hz
			Amplitude	3.77°	15.84°	5.39°
	With control-6 A	−7.13~5.58°	Amplitude	0.72°	4.63°	0.31°
			Control effect	80.90% −14.38 dB	70.77% −10.68 dB	94.25% −24.80 dB
II	Without control	−43.95~41.44°		0.06 Hz	0.12 Hz	0.18 Hz
			Amplitude	10.89°	28.15°	6.07°
	With control-6 A	−11.46~10.26°	Amplitude	2.01°	6.74°	0.32°
			Control effect	81.54% −14.68 dB	76.06% −12.42 dB	94.73% −25.56 dB
III	Without control	−44.20~42.41°		0.06 Hz	0.12 Hz	0.18 Hz
			Amplitude	11.31°	32.42°	8.33°
	With control-6 A	−13.18~9.03°	Amplitude	1.51°	7.31°	0.84°
			Control effect	86.65% −17.49 dB	77.45% −12.94 dB	89.92% −19.93 dB

The interference frequency is within 0.2 Hz. This frequency includes three main frequency signals: 0.06, 0.13 and 0.19 Hz. Specifically, 0.06 Hz is the fan rotation frequency; 0.13 and 0.19 Hz are close to frequency doubling. The interference amplitude is relatively large (within 25~45°), which is due to the very low interference frequency excitations. The frequency domain results show that the disturbance amplitude around 0.12 Hz is the largest, rather than 0.06 Hz, which is mainly due to the large flexibility of the plate. Especially, the full frequency band vibration suppression effect within 0.2 Hz is obvious, and the vibration suppression effect at 0.12 Hz (dominant frequency) is the best up to 12.94 dB (Experiment III).

The previous single-frequency excitation experiment was effective. However, the passive damping between the two permanent magnets may affect the vibration control effect of dual joints. Therefore, to highlight the performance of dual joints, it is of great necessity to investigate the semi-active vibration control effect under passive damping. The experimental process still uses the fan airflow excitation. In Figure 9, the motor output shaft is locked and PM1 remains stationary. The vibration control effect is depicted in Figure 14. The experimental results are summarized and compared in Table 6.
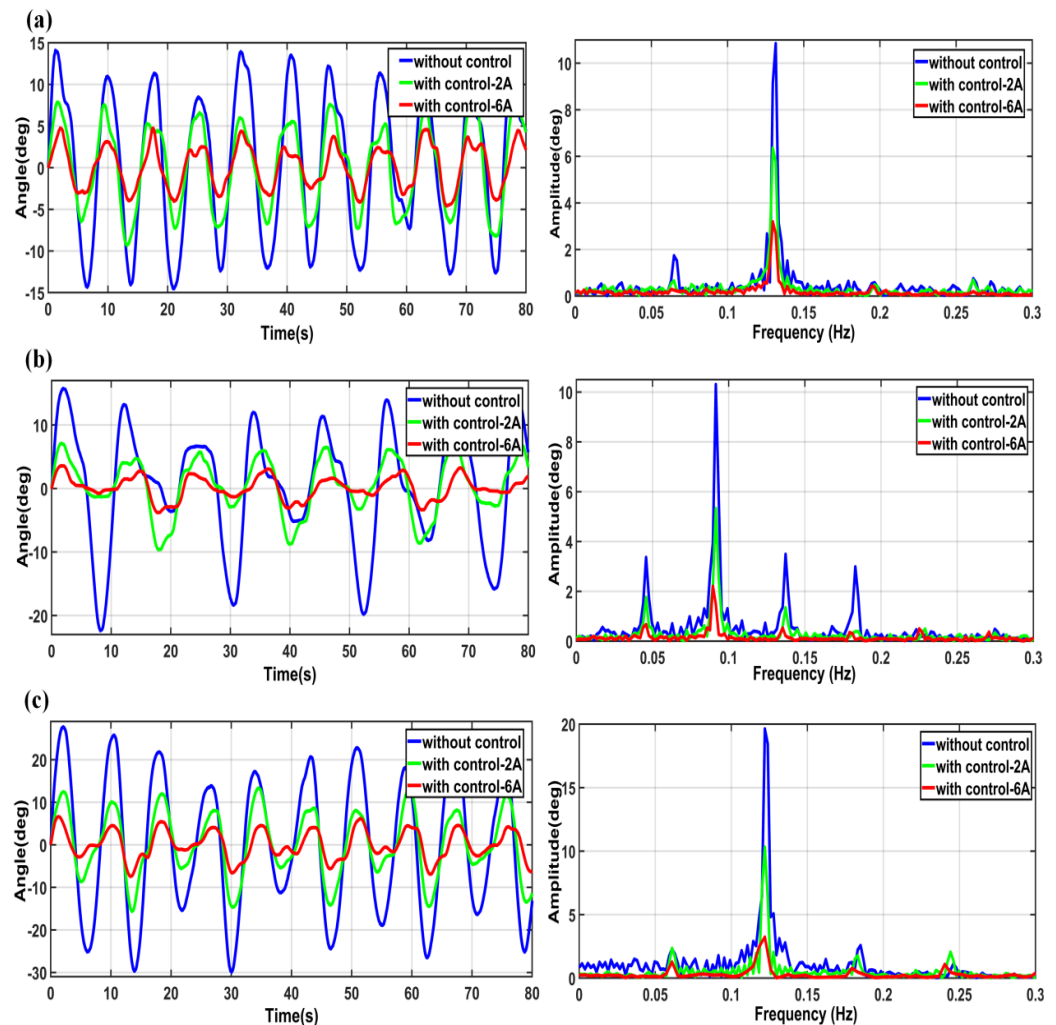

Figure 14. Vibration control experiments with passive damping: (**a**) Experiment I, (**b**) Experiment II and (**c**) Experiment III.

Table 6. Vibration control effect with passive damping.

Experiment	Amplitude			Major Frequency			
I	Without control	−14.51~14.08°		0.06 Hz		0.13 Hz	
			Amplitude	1.74°		10.84°	
	With control -6 A	−4.58~4.75°	Amplitude	0.29°		3.19°	
			Control effect	83.33% −15.56 dB		70.57% −10.62 dB	
II	Without control	−22.33~15.75°		0.05 Hz	0.09 Hz	0.14 Hz	0.18 Hz
			Amplitude	3.36°	10.30°	3.49°	2.99°
	With control -6 A	−3.78~3.56°	Amplitude	0.67°	2.21°	0.53°	0.35°
			Control effect	80.06% −14.01 dB	78.54% −13.37 dB	84.81% −16.37 dB	88.29% −18.63 dB
III	Without control	−29.89~27.73°		0.06 Hz	0.12 Hz	0.19 Hz	
			Amplitude	2.28°	19.63°	2.57°	
	With control -6 A	−7.40~6.64°	Amplitude	1.27°	3.23°	0.77°	
			Control effect	44.30% −5.08 dB	83.55% −15.67 dB	70.04% −10.47 dB	

Experimental results show that the interference frequency contains multiple frequency components. The frequency range is below 0.2 Hz; the interference amplitude is 14~30°. Compared with the experimental results by only using air flow excitation in Figure 13, the interference amplitude is reduced due to the passive damping effect. In Figure 14, with respect to interference amplitudes, the dominant frequencies are mainly 0.06, 0.12 and 0.18 Hz. Especially, four frequency components appear in Figure 14b. The full frequency band vibration suppression effect below 0.2 Hz is significant, especially at 0.18 Hz in Figure 14b, and the vibration reduction effect can reach 18.63 dB. This result further proves the semi-active vibration suppression effect of dual joints. In the case of multi-frequency excitations, due to the lower excitation frequency of the flexible plate, variable damping is the leading contributor with variable stiffness being the supplementary.

4.4. Comparative Analysis

In Figure 15, some comparisons of the numerical and experimental results are made under single-frequency excitation.

The frequency of the interference signal is 0.244, 0.282 and 0.343 Hz, respectively. For the time domain response, the interference signals in the simulation and experiment are primarily identical; however, there is a tiny difference in the control effect, particularly in the case of DC-6 A. For the frequency domain response, there is also a minor difference in the interference signals and control effect between the simulation and experiment.

The following are the principal reasons for the discrepancy between the experimental and simulation results: (1) the time domain signal generated by the self-built non-contact permanent magnet vibration exciter is not satisfactorily robust, and the angle signal acquired by the angular sensor may not be able to completely capture the real-time perturbation, thereby influencing the actual output of the joint itself. (2) Due to fabrication and construction imperfections, there exists clearance among the primary parts of the experimental prototype, which inevitably impacts the joint output rotation angle.
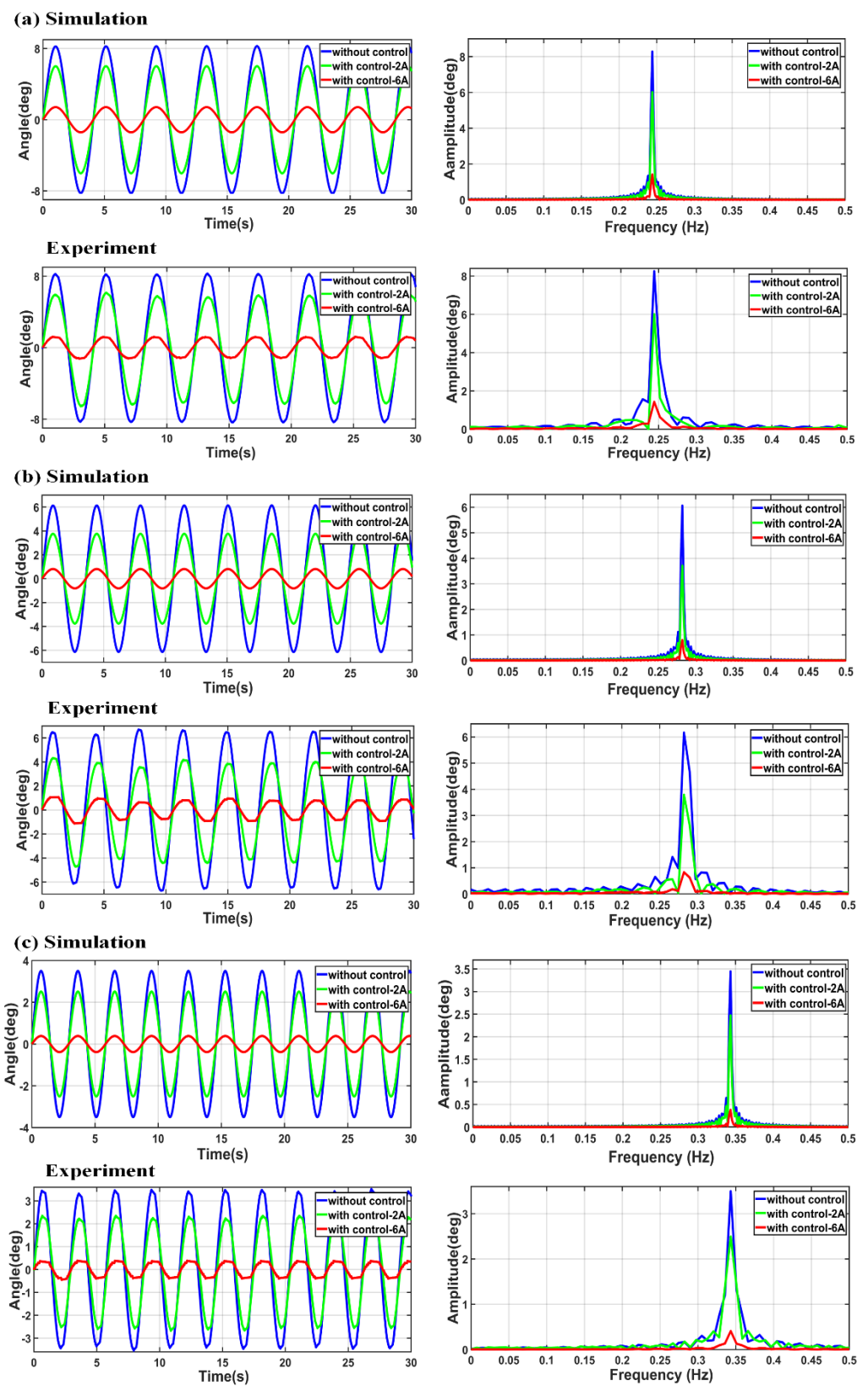
Figure 15. Comparative results of vibration control: (**a**) 0.244 Hz; (**b**) 0.282 Hz; and (**c**) 0.343 Hz.

5. Conclusions

To conclude, a new electromagnetic joint actuator for vibration control with tunable magnetically controlled stiffness/damping is proposed. The variable stiffness stems from the fact that when the adjusting coils of the joint mechanism are supplied with DC power, the output torque of the joint is nearly linear with the rotation angle. The variable damping derives from the eddy current damping, which results from the relative motion between the permanent magnet rotor and the joint stator core. Moreover, the greater the joint loading current and the rotating speed, the greater the eddy current damping torque.

Firstly, the tuning mechanism of the joint stiffness/damping parameters are explained for the coupling system of dual joints and a single flexible plate. The coupling dynamic equations are acquired by adopting the Lagrange equation and the assumed mode approach. Then, the semi-active vibration control simulations are conducted. The frequency-shift effect of the system is studied for the variable stiffness joint. Finally, the experimental platform of dual joints and a single flexible plate is built. The non-contact permanent magnet excitation is employed at the root of the flexible plate to simulate the single-frequency excitation. The non-contact airflow excitation is imposed on the surface of the flexible plate to simulate the multi-frequency excitation. The experimental results indicate that, for dual joints and a single flexible plate system, in the range of 0.06–0.343 Hz, magnetic-controlled damping dominates and magnetic-controlled stiffness is auxiliary. The primary reason is the fact that when dual joints are loaded with DC-2 A, the external excitation frequency is less when compared with the natural frequency of the system. There is no obvious effect of magnetic-controlled stiffness of the system. In addition, it is also experimentally verified that the dual joint actuation has good synchronization. In conclusion, the proposed control method is simple and effective. Only through the joint actuation, the low-frequency vibration of the flexible plate can be efficiently hindered, and the plate surface does not need any other intelligent equipment.

Furthermore, this study focuses on the basic research on the common problems abstracted from solar panel structures in space microgravity environment, which is realized by a scaled flexible plate model. The theoretical simulations and experimental verifications are adopted, and the semi-active vibration control effect of magnetic joints is demonstrated by building an experimental platform. The above-stated research results are significant for guiding the vibration attenuation of flexible space solar panels.

Author Contributions: Conceptualization, methodology, writing—original draft, W.H.; data curation, software, writing review & editing, J.W.; validation, supervision, formal analysis, Q.Z.; visualization, project administration, J.S.; investigation, funding acquisition, X.Z. All authors have read and agreed to the published version of the manuscript.

Institutional Review Board Statement: The study did not require ethical approval.

Informed Consent Statement: Not applicable.

Data Availability Statement: Not applicable.

Conflicts of Interest: The authors declare no conflict of interest.

References

1. Azadi, E.; Fazelzadeh, S.A.; Azadi, M. Thermally induced vibrations of smart solar panel in a low-orbit satellite. *Adv. Space Res.* **2017**, *59*, 1502–1513. [CrossRef]
2. Alkomy, H.; Shan, J. Modeling and validation of reaction wheel micro-vibrations considering imbalances and bearing disturbances. *J. Sound Vib.* **2021**, *492*, 115766. [CrossRef]
3. Guo, J.; Geng, Y.; Wu, B.; Kong, X. Vibration suppression of flexible spacecraft during attitude maneuver using CMGs. *Aerosp. Sci. Technol.* **2018**, *72*, 183–192. [CrossRef]
4. Cao, Y.; Cao, D.; He, G.; Ge, X.; Hao, Y. Modelling and vibration analysis for the multi-plate structure connected by nonlinear hinges. *J. Sound Vib.* **2020**, *492*, 115809. [CrossRef]

5. Li, Y.; Wang, C.; Huang, W. Rigid-flexible-thermal analysis of planar composite solar array with clearance joint considering torsional spring, latch mechanism and attitude controller. *Nonlinear Dyn.* **2019**, *96*, 2031–2053. [CrossRef]

6. Li, D.X.; Liu, W.; Lei, Y.J.; Sun, X.Y. Dynamic model for large multi-flexible-body space structures. *Int. J. Struct. Stab. Dyn.* **2014**, *14*, 1350072. [CrossRef]

7. Kong, Y.; Huang, H. Design and experiment of a passive damping device for the multi-panel solar array. *Adv. Mech. Eng.* **2017**, *9*, 1687814016687965. [CrossRef]

8. Maly, J.R.; Reed, B.B.; Viens, M.J.; Parker, B.H.; Pendleton, S.C. Life cycle testing of viscoelastic materials for Hubble Space Telescope solar array 3 damper. In Proceedings of the Smart Structures and Materials, San Diego, CA, USA, 3–6 March 2003; Volume 5052, pp. 128–141.

9. Kienholz, D.A.; Pendleton, S.C.; Richards, K.E., Jr.; Morgenthaler, D.R. Demonstration of solar array vibration suppression. In Proceedings of the 1994 North American Conference on Smart Structures and Materials, Orlando, FL, USA, 14–16 February 1994; Volume 2193, pp. 59–72.

10. Sales, T.P.; Rade, D.A.; de Souza, L.C.G. Passive vibration control of flexible spacecraft using shunted piezoelectric transducers. *Aerosp. Sci. Technol.* **2013**, *29*, 403–412. [CrossRef]

11. Zhang, M.; Xu, F. Tuned mass damper for self-excited vibration control: Optimization involving nonlinear aeroelastic effect. *J. Wind Eng. Ind. Aerodyn.* **2021**, *220*, 104836. [CrossRef]

12. Zhang, M.; Wu, T.; Øiseth, O. Vortex-induced vibration control of a flexible circular cylinder using a nonlinear energy sink. *J. Wind. Eng. Ind. Aerodyn.* **2022**, *229*, 105163. [CrossRef]

13. Zheng, Y.; Zhang, X.; Luo, Y.; Zhang, Y.; Xie, S. Analytical study of a quasi-zero stiffness coupling using a torsion magnetic spring with negative stiffness. *Mech. Syst. Signal Process.* **2018**, *100*, 135–151. [CrossRef]

14. Shi, X.; Zhu, S.; Li, J.-Y.; Spencer, B.F. Dynamic behavior of stay cables with passive negative stiffness dampers. *Smart Mater. Struct.* **2016**, *25*, 75044. [CrossRef]

15. Shi, X.; Zhu, S.; Spencer, B.F., Jr. Experimental study on passive negative stiffness damper for cable vibration mitigation. *J. Eng. Mech.* **2017**, *143*, 4017070. [CrossRef]

16. Shi, X.; Zhu, S.; Nagarajaiah, S. Performance Comparison between Passive Negative-Stiffness Dampers and Active Control in Cable Vibration Mitigation. *J. Bridge Eng.* **2017**, *22*, 4017054. [CrossRef]

17. Abdeljaber, O.; Avci, O.; Inman, D.J. Active vibration control of flexible cantilever plates using piezoelectric materials and artificial neural networks. *J. Sound Vib.* **2016**, *363*, 33–53. [CrossRef]

18. Qiu, Z.C.; Wang, X.F.; Zhang, X.M.; Liu, J.G. A novel vibration measurement and active control method for a hinged flexible two-connected piezoelectric plate. *Mech. Syst. Signal Process.* **2018**, *107*, 357–395. [CrossRef]

19. Li, D.; Jiang, J.; Liu, W.; Fan, C. A New Mechanism for the Vibration Control of Large Flexible Space Structures with Embedded Smart Devices. *IEEE/ASME Trans. Mechatron.* **2014**, *20*, 1653–1659. [CrossRef]

20. Xu, R.; Li, D.; Jiang, J. An online learning-based fuzzy control method for vibration control of smart solar panel. *J. Intell. Mater. Syst. Struct.* **2015**, *26*, 2547–2555. [CrossRef]

21. Xie, Y.; Shi, H.; Bi, F.; Shi, J. A MIMO data driven control to suppress structural vibrations. *Aerosp. Sci. Technol.* **2018**, *77*, 429–438. [CrossRef]

22. Wang, J.; Li, D. Experiments study on attitude coupling control method for flexible spacecraft. *Acta Astronaut.* **2018**, *147*, 393–402. [CrossRef]

23. Gol Zardian, M.; Moslemi, N.; Mozafari, F.; Gohari, S.; Yahya, M.Y.; Burvill, C.; Ayob, A. Flexural and free vibration control of smart epoxy composite beams using shape memory alloy wires actuator. *J. Intell. Mater. Syst. Struct.* **2020**, *31*, 1557–1566. [CrossRef]

24. Gohari, S.; Mozafari, F.; Moslemi, N.; Mouloodi, S.; Alebrahim, R.; Ahmed, M.; Abdi, B.; Sudin, I.; Burvill, C. Static and dynamic deformation response of smart laminated composite plates induced by inclined piezoelectric actuators. *J. Compos. Mater.* **2022**, *56*, 3269–3293. [CrossRef]

25. Pu, Y.X.; Zhou, H.L.; Meng, Z. Multi-channel adaptive active vibration control of piezoelectric smart plate with online sec-ondary path modeling using PZT patches. *Mech. Syst. Signal Process.* **2019**, *120*, 166–179. [CrossRef]

26. Jiang, J.-P.; Li, D.-X. Optimal placement and decentralized robust vibration control for spacecraft smart solar panel structures. *Smart Mater. Struct.* **2010**, *19*, 85020. [CrossRef]

27. Jiang, J.P.; Li, D.X. Decentralized robust vibration control of smart structures with parameter uncertainties. *J. Intell. Mater. Syst. Struct.* **2011**, *22*, 137–147. [CrossRef]

28. Gripp, J.A.B.; Rade, D.A. Vibration and noise control using shunted piezoelectric transducers: A review. *Mech. Syst. Signal Process.* **2018**, *112*, 359–383. [CrossRef]

29. Zhu, Q.; Yue, J.Z.; Liu, W.Q.; Wang, X.D.; Chen, J.; Hu, G.D. Active vibration control for piezoelectricity cantilever beam: An adaptive feed-forward control method. *Smart Mater. Struct.* **2017**, *26*, 47003. [CrossRef]

30. Lin, J.; Zheng, Y.B. Vibration suppression control of smart piezoelectric rotating truss structure by parallel neuro-fuzzy control with genetic algorithm tuning. *J. Sound Vib.* **2012**, *331*, 3677–3694. [CrossRef]

31. Ma, B.; Qiu, Z.-C.; Zhang, X.-M.; Han, J.-D. Experiments on resonant vibration suppression of a piezoelectric flexible clamped–clamped plate using filtered-U least mean square algorithm. *J. Intell. Mater. Syst. Struct.* **2014**, *27*, 166–194. [CrossRef]

32. Casciati, F.; Rodellar, J.; Yildirim, U. Active and semi-active control of structures-theory and applications: A review of recent advances. *J. Intell. Mater. Syst. Struct.* **2012**, *23*, 1181–1195. [CrossRef]

33. Pu, H.; Yuan, S.; Peng, Y.; Meng, K.; Zhao, J.; Xie, R.; Huang, Y.; Sun, Y.; Yang, Y.; Xie, S.; et al. Multi-layer electromagnetic spring with tunable negative stiffness for semi-active vibration isolation. *Mech. Syst. Signal Process.* **2019**, *121*, 942–960. [CrossRef]

34. Hu, W.; Gao, Y.; Sun, X.; Yang, Y.; Yang, B. Semi-active vibration control of a rotating flexible plate using stiffness and damping actively tunable joint. *J. Vib. Control* **2019**, *25*, 2819–2833. [CrossRef]

35. Zhang, J.; Lu, S.; Zhao, L. Modeling and disturbance suppression for spacecraft solar array systems subject to drive fluctuation. *Aerosp. Sci. Technol.* **2020**, *108*, 106398. [CrossRef]

36. Hu, W.; Gao, Y.; Yang, B. Semi-active vibration control of two flexible plates using an innovative joint mechanism. *Mech. Syst. Signal Process.* **2019**, *130*, 565–584. [CrossRef]

37. Singiresu, S.R. *Mechanical Vibrations*; Addison Wesley: Boston, MA, USA, 1995.